Geology, Geophysics & Environment 2023, vol. 49 (3): 281–298

Rock type discrimination using Landsat-8 OLI satellite data in mafic-ultramafic terrain

Kuppusamy Tamilarasan[1], Siddan Anbazhagan[2], Sundararajan Ranjithkumar[3]

[1] *Periyar University, Centre for Geoinformatics and Planetary Studies, Salem, Tamil Nadu, India, e-mail: ktamilarasan05@gmail.com, ORCID ID: 0000-0001-5880-4093*
[2] *Periyar University, Centre for Geoinformatics and Planetary Studies, Salem, Tamil Nadu, India, e-mail: anbu02@gmail.com (corresponding author), ORCID ID: 0000-0003-3366-1895*
[3] *Periyar University, Centre for Geoinformatics and Planetary Studies, Salem, Tamil Nadu, India, e-mail: georanjith1993@gmail.com, ORCID ID: 0000-0001-9727-2309*

© 2023 Author(s). This is an open access publication, which can be used, distributed and re-produced in any medium according to the Creative Commons CC-BY 4.0 License requiring that the original work has been properly cited.

Received: 20 February 2023; accepted: 6 July 2023; first published online: 12 September 2023

Abstract: The mafic-ultramafic terrain of the Bhavani complex in southern India is considered for lithological mapping. The Landsat-8 OLI satellite data was used for the interpretation of different rock types in the study area. The satellite data were digitally processed using ENVI 5.6 image processing software. In the OLI data, excluding bands 8 and 9, the remaining seven bands were used for the generation of colour composite images, band ratios, principal component analysis and SVM classification. Reflectance spectral measurements were carried out in laboratory conditions for five rock samples collected from the study area. The XRF analysis was carried out to estimate the composition of major oxides present in the rock samples. The results obtained from XRF analysis were compared with the rock spectra in characterizing the spectral features of the rock types. The colour composite images (B543, B567, B456, and B457), PCA composite image (PC312 and PC456), band ratios (BR5/5 and BR4/3), colour composite images from band ratios, and SVM classified output are useful in delineation various rock types in the terrain.

Keywords: remote sensing, Landsat-8, lithology, ultramafic, spectra, SVM classification

INTRODUCTION

Remote sensing techniques are being continuously utilized for various geological applications such as lithological mapping, mineral exploration, landforms studies, engineering projects and groundwater studies. In the last few decades, remote sensing data were successfully applied for mapping rock types and mineral deposits (Abrams 1984, Sultan et al. 1987, Drury 1990, Glikson & Creasey 1995, Krishnamurthy 1997, Sabins 1999, Abdeen et al. 2001, Anbazhagan et al. 2006, 2012, Pour et al. 2018, Maheswaran et al. 2019, Kamel et al. 2022). In the earlier period, aerial photographs and Landsat MSS data were adopted for the interpretation of geological features (Goetz & Rowan 1981). Remote sensing applications in geology increased significantly after the commencement of the Earth resource satellite (Landsat) programme (Bhan et al. 1991). Landsat Thematic Mapper (TM) images have been widely used for geological resource mapping for many years, particularly for the discrimination of rock types, structural mapping, and locating alteration minerals (Chavez et al. 1991, Yesou et al. 1993). Abrams et al. (1983) have utilized Landsat MSS and simulated Landsat-4 TM data to evaluate the

mapping capabilities of copper deposits, discrimination of lithologies, hydrothermal alteration, and structural mapping. Landsat TM principal component analysis was carried out by Loughlin (1991) for the delineation of alteration mineral zones in the Roberts Mountains, Nevada (Yesou et al. 1993) have used SPOT panchromatic image merged with Landsat TM data for the structural mapping and delineation of lithological boundaries between granitic domes and sedimentary formations. The medium-resolution IRS P6 LISS III satellite data was used for the interpretation of the lithology and structure of the Kadavur basin, India (Maheswaran et al. 2019). Zhang et al. (2007) have processed the ASTER data for the exploration of gold mineral deposits through the interpretation of lithology and mineralogical information.

In comparison with Landsat-7 ETM satellite data, Landsat-8 (OLI) improved the capability of the sensor by adding two more spectral bands (Roy et al. 2014, Mwaniki et al. 2015). The optical index factor (OIF) of satellite data was used to improve the quality of images for the interpretation of geology (Prinz 1996, Gad & Kusky 2007). The correlation coefficient and OIF have been used to optimally select the colour composites, PCA combinations and band ratios of Landsat-8 OLI. The supervised classification output prominently supports for geological mapping of Neo-proterozoic basement rocks in the central-eastern desert of Egypt (Kamel et al. 2022). Landsat-8 OLI Data was successfully used to extract gossan zones in arid regions of the Eastern Arabian Shield (Gahlan & Ghrefat 2018). In the present study, the Bhavani complex in southern India was selected for mapping various rock types using remote sensing techniques. The digitally processed Landsat-8 OLI satellite data was used for the discrimination of various rock types.

THE GEOLOGICAL SETTING OF THE BHAVANI COMPLEX

The southern peninsular of India encompasses a variety of geological, geochemical, structural, and metamorphic features and has undergone many stages of magmatism, primarily in the Proterozoic and late Palaeozoic periods (Bhattacharya 2010). The study area, the 'Bhavani complex', is part of the Mettupalaiyam mafic-ultramafic complex located in the western part of Tamil Nadu, India. The region of study covers approximately 300 km^2 area and falls in between the eastern longitude of 77°00'E to 77°20'E and the northern latitude of 11°18'N to 11°28'N (Fig. 1).

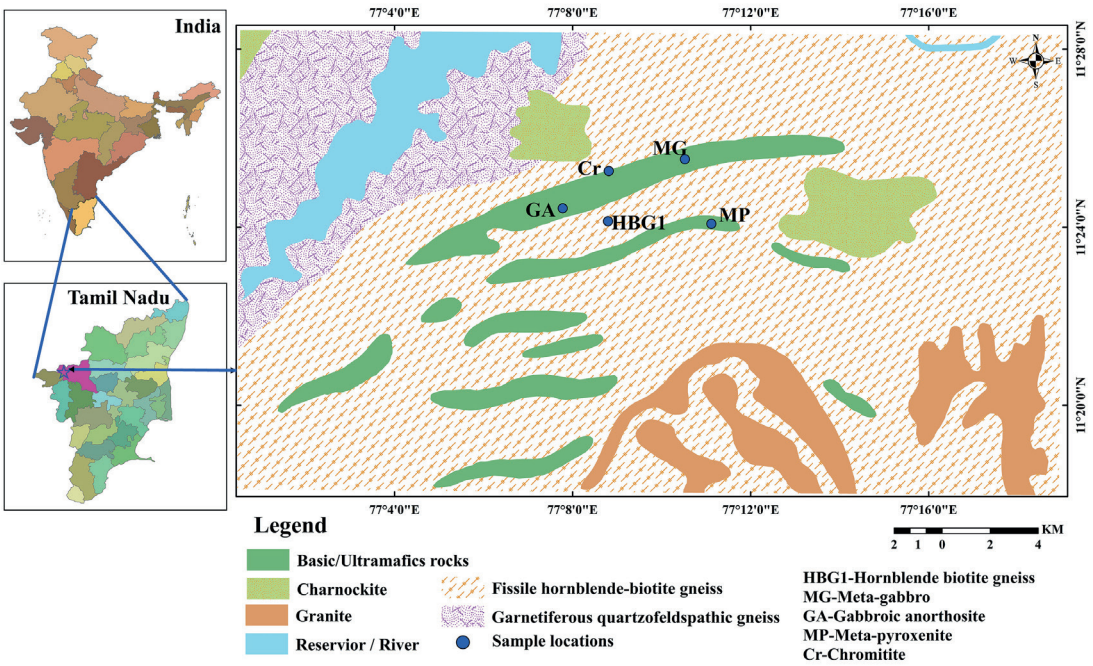

Fig. 1. Location and geology map of Bhavani complex, Southern India (GSI)

Regionally, the Bhavani complex is associated with Southern Granulitic Terrain (SGT) and is part of the major Cauvery Suture Zone (CSZ) (Satyanarayanan et al. 2011). The complex is covered by a fragmented sequence of mafic-ultramafic rocks, surrounded by hornblende biotite gneiss, granites, charnockites, and quartzo feldspathic gneiss. The mafic-ultramafic formation outcropped as E-W trending discontinues lensoidal bodies. The formation comprises gabbro, metagabbro, gabbroic anorthosite, meta-pyroxenite and chromitite. The mafic-ultramafic terrain dates from the Archean period and has undergone a high degree of granulite facies metamorphism and deformation at about 2.9 Ga, based on Sm-Nd dating (Rao et al. 1996). Geologically, the hornblende biotite gneiss and charnockite are covered by the Bhavani gneissic complex and the charnockite group, respectively. Geoscientists from the Geological Survey of India have conducted investigations in this region for Cu-Ni-PGE mineralization (Gopalakrishnan & Shanmugam 1995, Prabhakar et al. 2012).

METHODOLOGY

Atmospheric correction of OLI data

The Landsat-8 Operational Land Imager (OLI) satellite data downloaded from the USGS Earth Explorer data product (https://earthexplorer.usgs.gov) was used for the interpretation of various rock types in the Bhavani complex. The Landsat-8 OLI data for the study area was captured on March 13, 2019. The Landsat-8 ID is (LC08_L1TP_144052_20190313_20200829_02_T1). The satellite scene carries path 144 and row 052 numbers. The Landsat-8 OLI data have nine spectral bands covering visible, NIR and SWIR spectra. The specifications of Landsat-8 OLI data are given in Table 1.

The ENVI 5.6 image processing software was used for processing the Landsat-8 OLI data. The atmospheric effects like scattering and absorption in the satellite data need to be corrected before processing it for various applications and interpretations. The atmospheric correction involves the removal of the atmospheric effects on the reflectance value in the satellite image. The quick atmospheric correction (QUAC) module available in ENVI 5.6 software was used to reduce the atmospheric effect and transform the digital numbers (DN) into reflectance data. QUAC considered atmospheric correction parameters directly from the observed pixel spectra in an image without supplementary data. The QUAC was adopted based on the average reflectance of a group of assorted material on-scene independents, determined empirically (Bernstein et al. 2012). The L1 OLI metadata was imported as input data in the QUAC module and obtained atmospherically corrected output data.

Table 1
Specification of Landsat-8 Operational Land Imager (OLI)

Bands	Wavelength [μm]	Resolution [m]
Band 1 – Coastal aerosol	0.43–0.45	30
Band 2 – Blue	0.45–0.51	30
Band 3 – Green	0.53–0.59	30
Band 4 – Red	0.64–0.67	30
Band 5 – Near Infrared (NIR)	0.85–0.88	30
Band 6 – SWIR 1	1.57–1.65	30
Band 7 – SWIR 2	2.11–2.29	30
Band 8 – Panchromatic	0.50–0.68	15
Band 9 – Cirrus	1.36–1.38	30

Optical index factor (OIF) and band combination

The advantage of band combination is that multiple images (three) can be displayed and interpreted simultaneously. Creating colour composites in the image processing technique is an effective mode of demonstration of multispectral images (Buchanan 1979). A number of colour models are being used in band combinations. The RGB is a well-known model in which red, green and blue are the three primary additive colours used for colour image display (Gupta 2017). In the RGB model, three input images are projected simultaneously, i.e. one in red, the second in green and the third in blue additive colour. The variation in digital numbers for different pixels in the three input images collectively leads to variation in output colours. The RGB colour image provides enhanced information for interpretation. The RGB colour images can be created by combining bands from

the visible, NIR, and SWIR spectra (Evans 1988, Crósta & Moore 1990). The false colour composite (FCC) image is a widely adopted composite image for lithology interpretation. The standard FCC is generated using multispectral images of green, red, and near-IR bands projected in blue, green and red colour filters. The FCC image was created for the study area using Landsat-8 OLI B5, B4, and B3 in red, green, and blue display planes. The true (natural) colour composite (TCC) image was created with the help of B4, B3, and B2 in the RGB combination. In Landsat-8 OLI data, we have selected seven bands (B1 to B7) for band combinations. In this case, the selection of a suitable band combination for good interpretation is a difficult task. The optical index factor (OIF) technique developed by Chavez et al. (1982) is useful in the selection of the best combination by quantitative evaluation of the image statistics. The OIF calculate the statistics of every possible three bands extracted through RGB filters. The process avoids the time-consuming visual inspection of the number of RGB colour combinations (Beauchemin & Fung 2001). Based on the value of OIF, the most favourable band combinations were ranked (Chavez et al. 1982, 1984). The ranking reflects the amount of total variance and correlation between various bands. In the present case, ILWIS 3.3 software was used to calculate OIF index values for band combinations. The seven-band Landsat-8 OLI data were imported into ILWIS software. The map list was used as input data for the correlation matrix module, and OIF index values were calculated. The OIF ranking band combinations are listed in Table 2. A set of three bands with a maximum value of OIF was selected for the generation of a clour composite image with RGB filters.

Table 2
The optimum index factor (OIF) for ranking the combination of bands

Rank	Band-triplet	OIF
1	567	0.12
2	456	0.11
3	457	0.11
4	156	0.11
5	157	0.11

Principal component analysis (PCA)

The principal component analysis (PCA) was carried out from Landsat-8 OLI seven-band data. The objective of PC analysis is to create uncorrelated output bands, separate noise components, and reduce the dimensionality of the multispectral data (Loughlin 1991, Ciampalini et al. 2013, Gahlan & Ghrefat 2018). In the PCA output, a new set of orthogonal axes developed with their origins at the data means and rotations that maximize variance in the data. The PC analysis was carried out using ENVI 5.6 image processing software. The atmospherically corrected seven-band data were used as the input file in the 'PCA rotation' module available in the 'Transform' toolbox in the ENVI software. The output file generated seven sets of PCA bands, such as PC1, PC2, PC3, PC4, PC5, PC6, and PC7. Usually, the first three bands carry maximum information, and the last band holds noise data. The seven PC output bands were combined through RGB filters, and PCA composite images were generated for the interpretation of rock types.

Band ratios

Band ratio is one of the important image processing techniques which enhances the surface features in multispectral images. The procedure is used to reduce the effect of illumination and topography to provide a contrast spectral signature in the images (Crane 1971, Holben & Justice 1981, Jensen 1996, Gupta 2017). The new output image is constructed by computing the ratio of the DN value of two input images. The Landsat-8 OLI seven-band data were used to derive all possible band ratio images for the study area. Different combinations of band ratio images were generated using the 'Band Algebra' tool available in ENVI 5.6 software. In this module, the numerator and denominator bands were assigned as input data and the output ratio image was obtained. The band ratio outputs 2/1, 3/2, 4/2, 4/3, 5/2, 5/4, 6/2, 6/3, 6/4, 6/5, 7/2, and 7/6 were used for further interpretation and band combinations. The output images 4/3 and 6/5 are displayed in the grey scale. The grey-scale ratio images show enhanced spectral signatures for different rock types.

SVM classifications

Support vector machines (SVM) is a significant machine learning classification procedure in the digital image processing of remote sensing data (Pal & Mather 2005). SVM is based on statistical learning theory and has the aim of determining the location of decision boundaries that produce the optimal separation of classes (Vapnik 1995). It has unique advantages in a limited sample, nonlinear and high dimensional pattern recognition. SVM is mostly used for the classification of remote sensing data and can achieve better results than other algorithms (Scheunders et al. 2018). The principle of SVM is to deal with complicated data classification by solving the optimization problem and finding the optimal classification hyperplane in the high-dimensional feature space. The SVM classification was successfully applied for vegetation and forest cover mapping by several workers (Huang et al. 2008, Su & Huang 2009). In the present case, SVM classification of Landsat-8 OLI data was carried out using ENVI 5.6 software to discriminate rock types in the study area. The training sets (region of interest-ROI) were generated for different lithologies such as mafic-ultramafic, granite, garnetiferrous quartzo feldspathic gneiss, hornblende biotite gneiss, and charnockite in the study region. The false colour composite image with B543 combination was used as a background image for extracting training pixels. The pure pixels were extracted after enlarging the composite image. The ROI was given as input data in the SVM classification module in the software and the polynomial Kernal type was adopted to obtain SVM classified output.

Chemical analysis

Fresh rock samples representing different lithologies were collected from the study area. The sample locations are shown in Figure 1. Using the XRF method, chemical analysis was carried out from five rock samples, including hornblende biotite gneiss, meta-gabbro, meta-pyroxenite, gabbroic anorthosite, and chromitite. The Rigaku XRF facility available at the Department of Earth Sciences, IIT Bombay, was utilized for the chemical analysis. The lumpsum rock samples were powdered into 75-micron grain size for chemical analysis. The chemical analysis was conducted for the estimation of major oxides, including SiO_2, Al_2O_3, CaO, MgO, Na_2O, K_2O, TiO_2, Fe_2O_3, MnO, and P_2O_5 (Table 3).

Reflectance spectral measurements

Reflectance spectra measured in the 350–2500 nm EMR spectrum provide diagnostic reflectance and absorption features for various rock types and minerals (Clark 1999). The reflectance spectral studies in remote sensing technique referred to as imaging spectroscopy (Ruiliang 2017), which is useful in geological applications including lithological mapping, mineral exploration and planetary geological studies (Anbazhagan et al. 2012, Bhattacharya et al. 2012, Kusuma et al. 2012, Chellamuthu Ranganathan & Siddan 2021, Tamilarasan et al. 2022). In the present context, lab spectral measurements were conducted on selected rock samples collected during the field visit at the Bhavani complex. The rock samples were collected from fresh outcrop sections and powdered into 75-micron sizes (Fig. 2).

Table 3
Major oxides in the rock samples were estimated through XRF analysis

Sample no.	Sample name	SiO_2	Al_2O_3	CaO	MgO	Na_2O	K_2O	TiO_2	Fe_2O_3	MnO	P_2O_5	Total
1	Hornblende biotite gneiss	70.50	14.60	3.08	0.709	4.84	2.09	0.39	3.27	0.066	0.093	99.63
2	Meta-gabbro	46.30	14.50	13.30	6.59	2.50	0.10	1.07	15.20	0.24	0.00	99.80
3	Gabbroic-anorthosite	66.10	14.90	4.51	3.14	2.24	3.19	0.64	5.12	0.00	0.00	99.84
4	Meta-pyroxenite	47.30	13.60	10.90	8.12	0.81	4.14	0.85	13.70	0.27	0.00	99.68
5	Chromitite	49.73	9.66	7.02	4.20	2.20	0.58	1.58	14.41	0.18	0.20	89.75

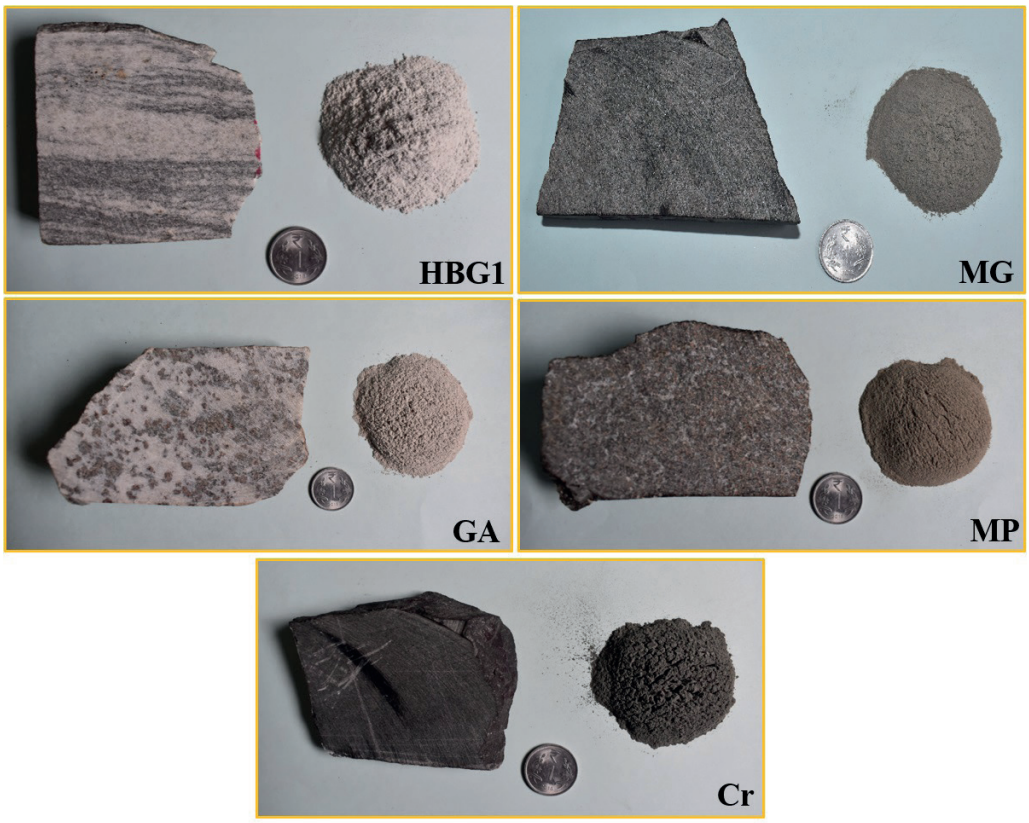

Fig. 2. *Rock samples including hornblende biotite gneiss (HBG1), meta-gabbro (MG), gabbroic anorthosite (GA), meta-pyroxenite (MP), and chromitite (Cr) from the Bhavani complex used for chemical analysis and spectral measurements. Powdered samples are shown, along with hand specimens*

The rock samples include hornblende biotite gneiss, meta-gabbro, meta-pyroxenite, gabbroic anorthosite, and chromitite. A ASD FieldSpec Pro® spectroradiometer was utilized to measure the reflectance spectra of the rocks under laboratory conditions. A tungsten lamp was used as an illumination source for spectral measurements under UV-visible, IR and SWIR spectra. For each rock sample, one spectral measurement was conducted. The spectra were plotted for all rock types using Origin Pro 8.5 software.

RESULTS AND DISCUSSION

FCC and interpretation of rock types

The Landsat-8 OLI satellite data were digitally processed and generated various output images for the discrimination of rock types in the mafic-ultramafic terrain of the Bhavani complex. The remote sensing-based interpretation was compared to the supplementary data like geology, rock spectra and geochemistry. The FCC output (B543 in RGB filters) provides a contrast colour signature between granitic gneiss (Gr-in bright) and hornblende biotite gneiss (Hbg) (Fig. 3). The mafic-ultramafic formations (M/Um) show prominent ridges in the middle and subdued surface level topography in the northern part of the study area. It is surrounded by hornblende biotite gneiss (Hbg) with an olive green colour signature. The canal-irrigated cultivated land (Cl) in the north-eastern part of the study area represents a red colour signature due to vegetation practices. The canal-irrigated area is mostly underlined by gneissic formation. The open forest covered with dark brown colour represents charnockite hills (Ch). The presence of the water body (Wb) in the reservoir shows a contrasting dark colour signature. The true colour composite image (Fig. 4) provided for the region of interest (ROI) for comparison with the FCC and other digitally processed output.

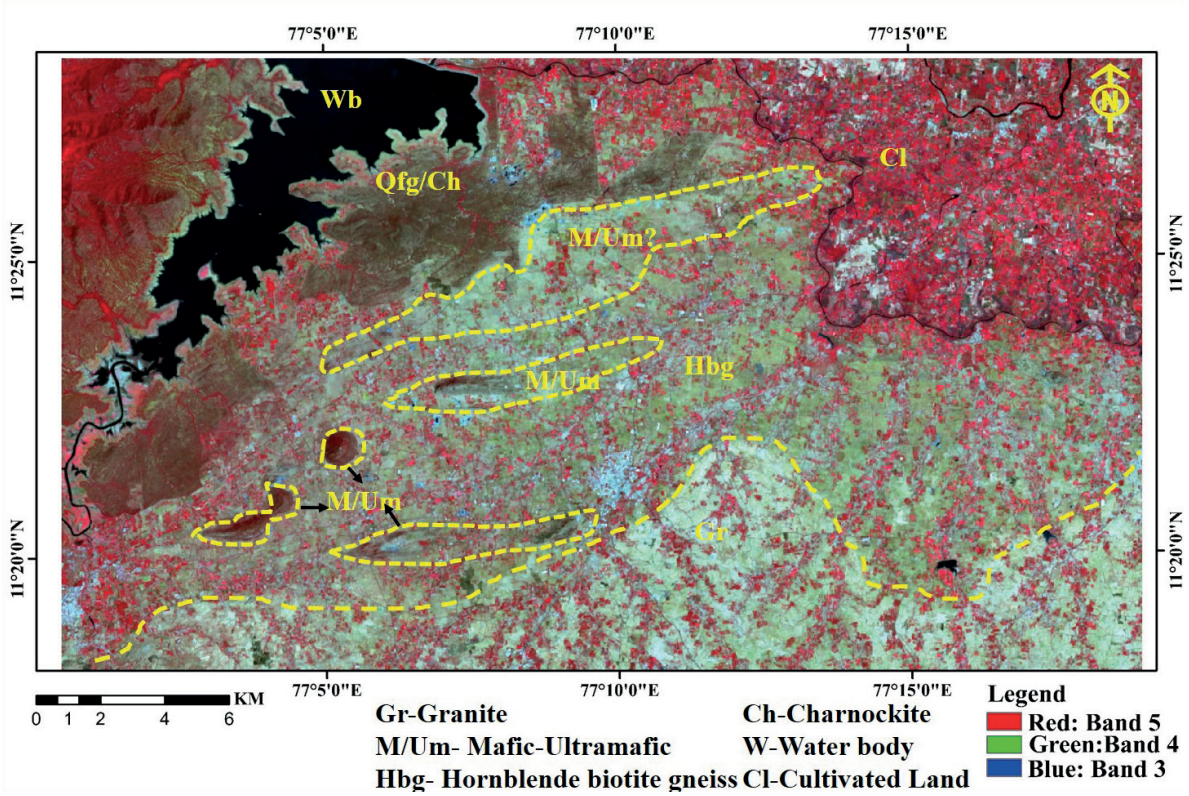

Fig. 3. *False colour composite image of Landsat-8 OLI bands B543 in RGB filters*

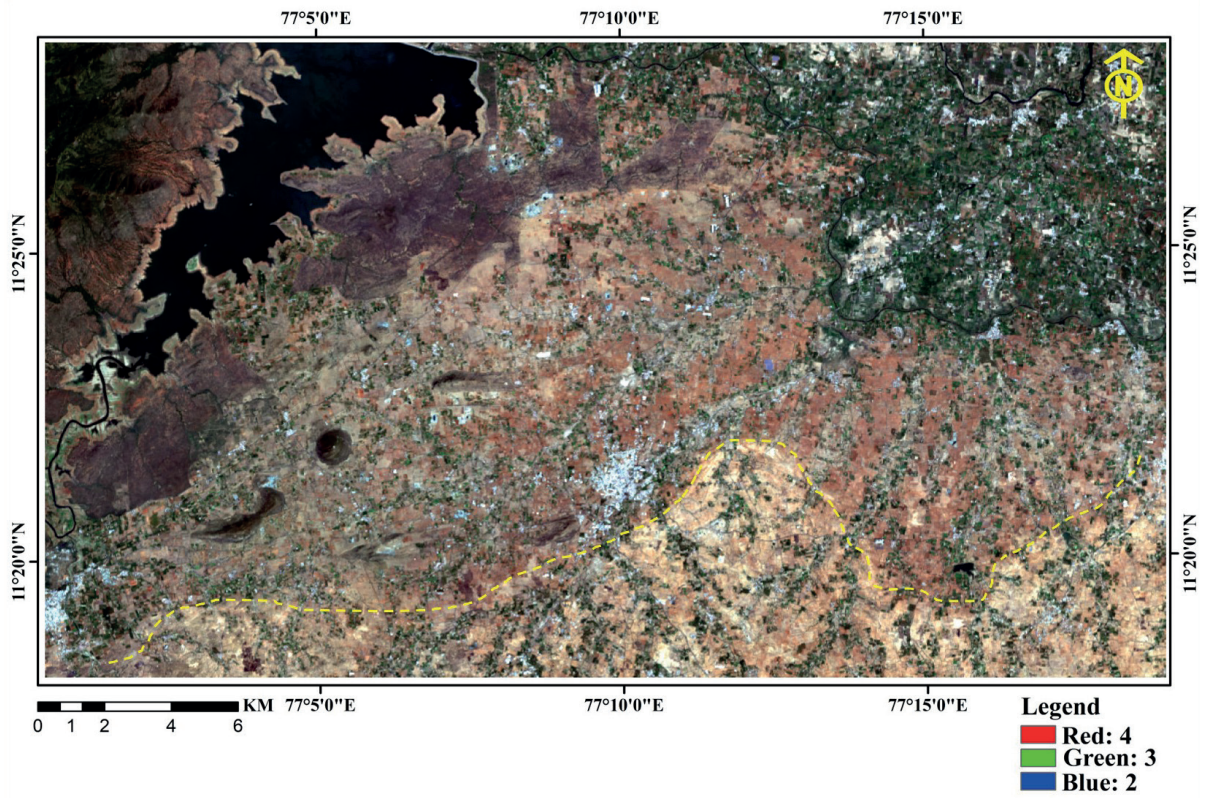

Fig. 4. *True colour composite image with B4, B3 and B2 for ROI*

In TCC, a contrast spectral signature was obtained between granitic gneiss and hornblende biotite gneiss. The mafic-ultramafic formation also shows prominent relief features in the terrain.

Band combination and rock-type delineation

The results obtained from OIF were used for the generation of band combination outputs. The set of three bands with a maximum value of OIF was selected for the generation of a colour composite image with RGB filters. The short-listed colour composite images B567, B456, and B457 show OIF index values of 0.12, 0.11, and 0.11, respectively. The colour composite images are helpful in the delineation of various rock types in the study area. The colour composite images B567, B456, and B457 provide enhanced spectral signatures for most of the lithologies like mafic-ultramafics (M/Um), gneiss (Hbg), granite (Gr), charnockite (Ch) and cultivated land (Cl) (Fig. 5A–C). The lithological contact between granite and gneiss is well exposed in all colour composite images. The surface level outcropping of the mafic-ultramafic (M/Um) formation near the charnockite formation shows a contrast spectral signature in B457 composite image (Fig. 5D). However, it shows poor contrast in B567 composite image.

Interpretation of PCA output

Principal component analysis is one of the widely adopted image-processing techniques for various geological applications, particularly for mapping of lithology and alteration mineral deposits (Loughlin 1991, Ruiz-Armenta & Prol-Ledesma 1998, Amer et al. 2010, Kumar et al. 2015). The PCA output bands (PC1 to PC7) in greyscale are not directly suitable to interpret rock types in the study area. Hence, the colour composite images were generated from PCA output bands for interpretation. Out of various combinations, we have identified that PC312 and PC456 are suitable for delineating rock types in the terrain (Figs. 6, 7).

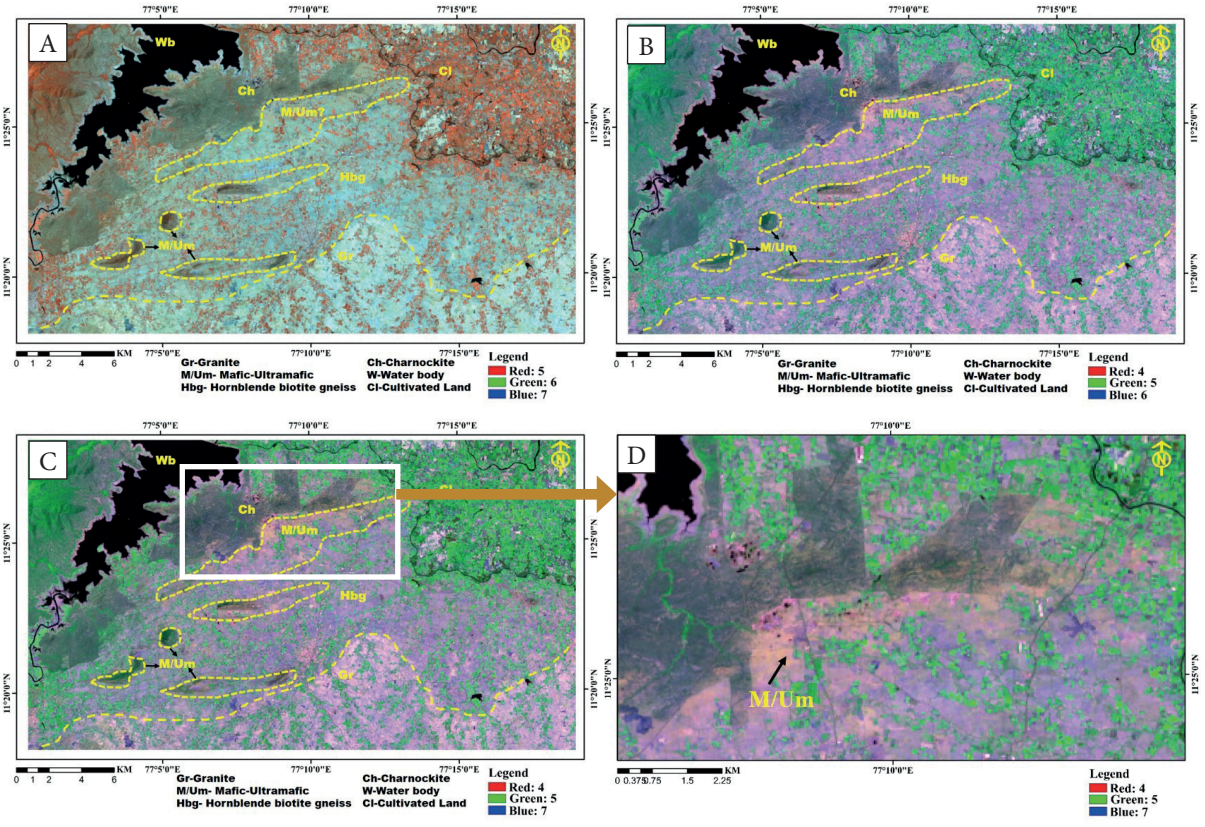

Fig. 5. The colour composite images of Landsat-8 OLI bands: A) B567; B) B456; C) B457; D) enlarged output of B457

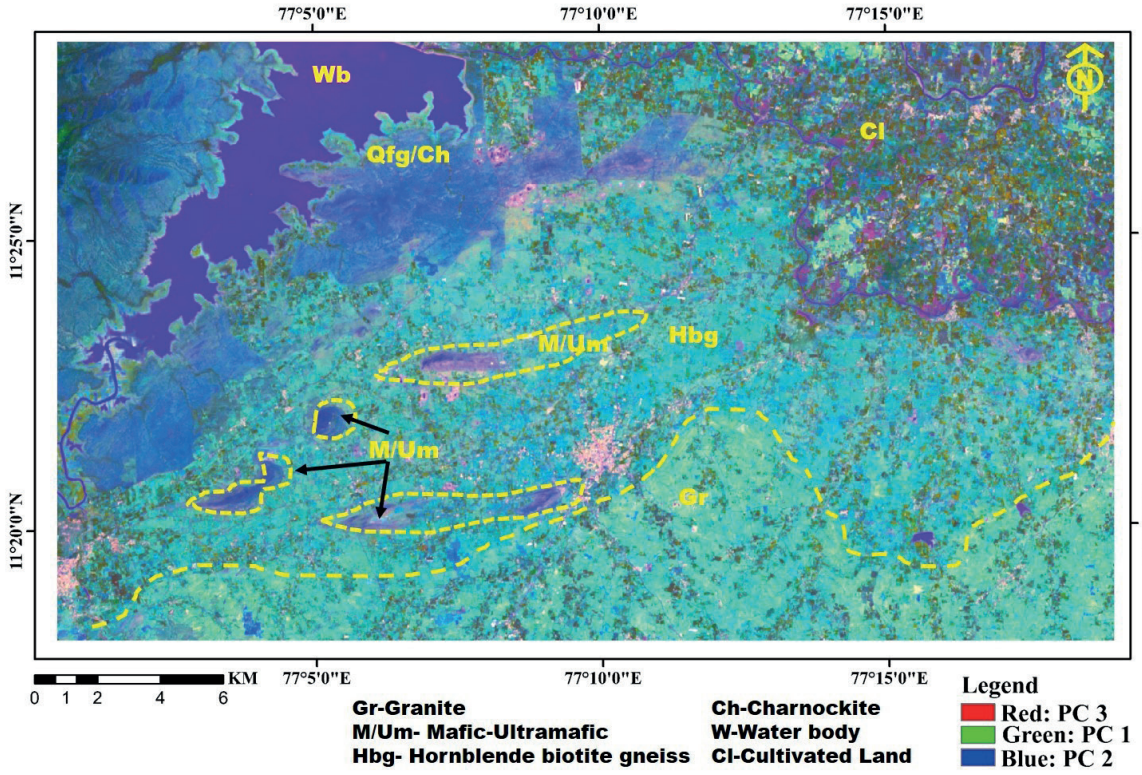

Fig. 6. *Principal component analysis of Landsat-8 OLI data band combination PC312 in RGB filters*

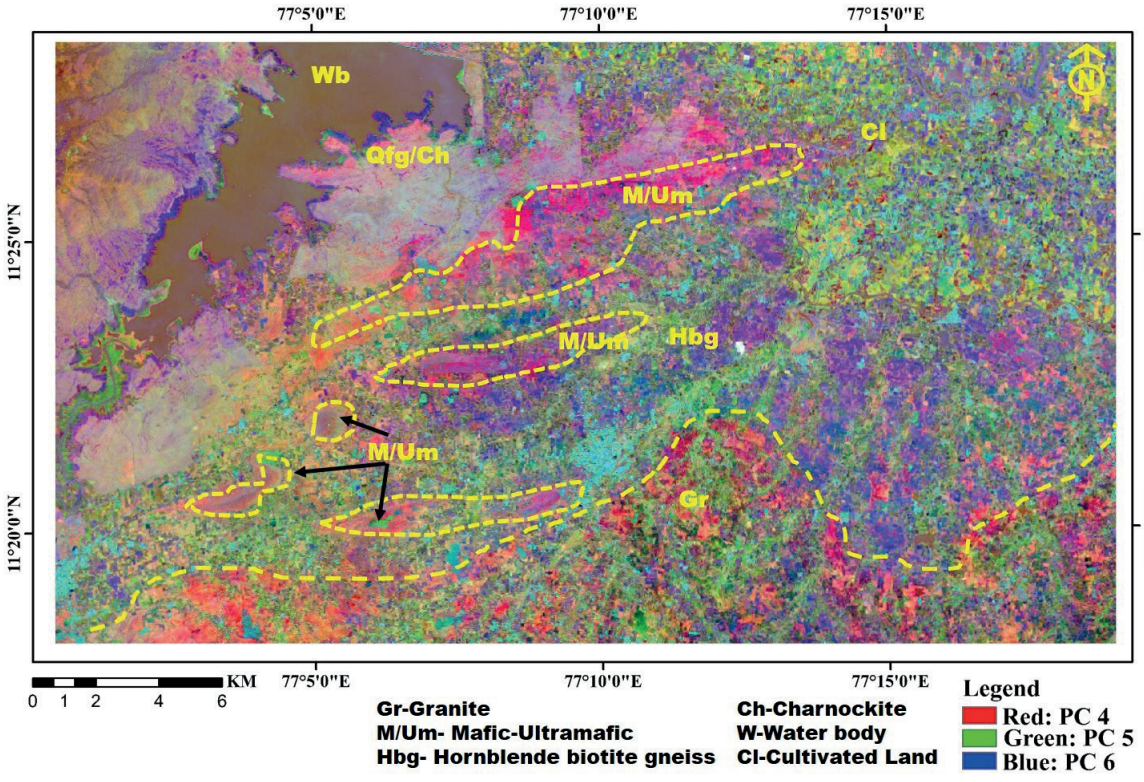

Fig. 7. *Principal component analysis of Landsat-8 OLI data band combination PC456 in RGB filters*

In PC312, the contrast colour signature was obtained between different rock types such as granite (Gr-aquamarine), gneiss (Hbg-cyan), mafic-ultramafic outcrops (M/Um-indigo), reserve forest zone underlined by charnockite and quartzo feldspathic gneiss (Qfg/Ch-royal blue in smooth texture), reservoir/water body (Wb-violet), and cultivation/vegetation (Cl-olive green). The boundary between different lithologies is fuzzy in the PC456 composite image. The surface level outcropping of mafic-ultramafic (M/Um-magenta) formation in the study area shows a contrast spectral signature in the PC456 composite image.

Band ratios in mapping rock types

The ratioed multispectral satellite data is also widely used for various geological applications (Abrams 1984, Satterwhite 1984, Kaufmann 1988, Gahlan & Ghrefat 2018, Abdelsalam et al. 2000). In the present case, of the various ratioed output images, only two images with greyscale like, BR6/5, and BR4/3 were considered (Fig. 8).

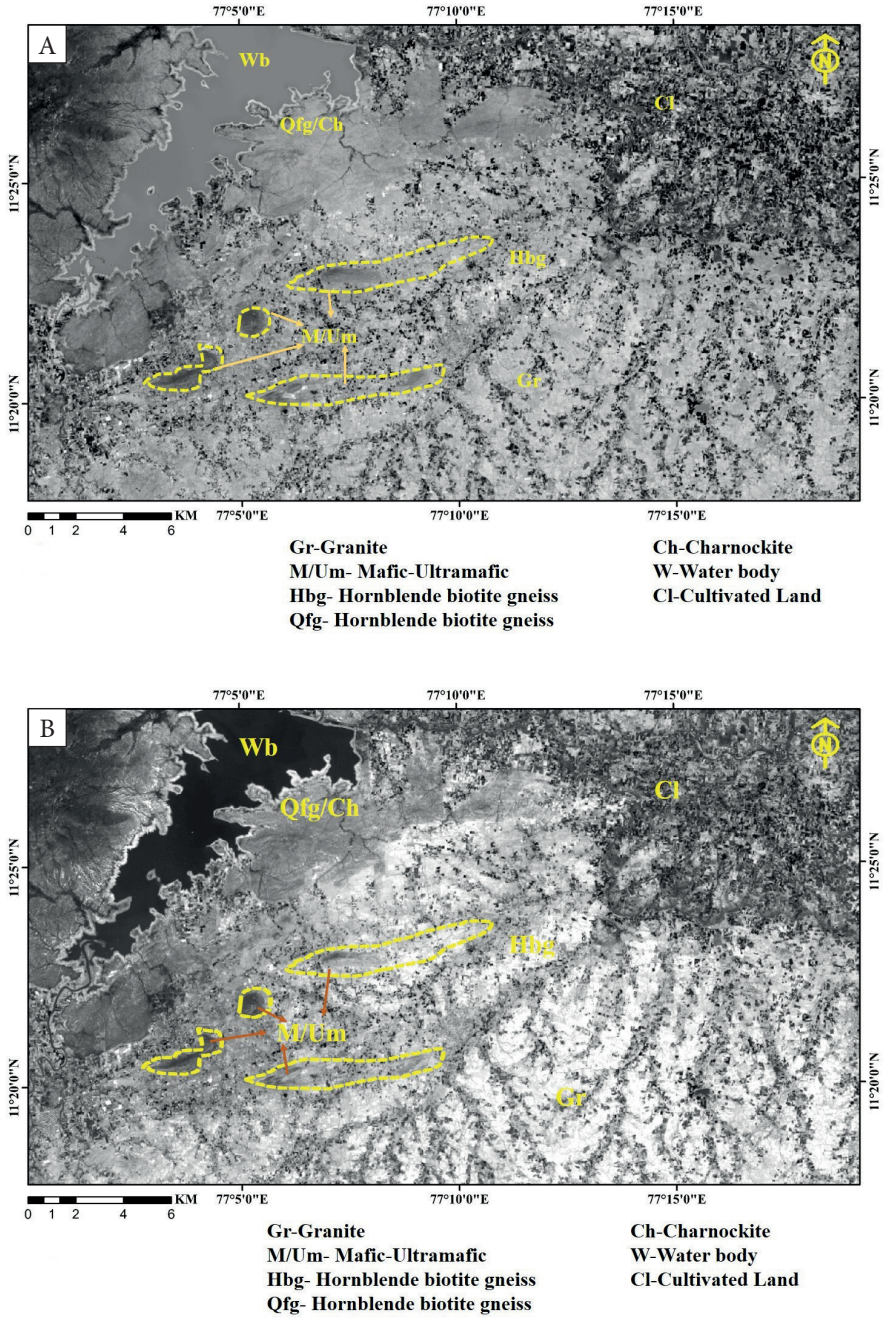

Fig. 8. *Band ratio images BR6/5 (A) and BR4/3 (B) show different rock types in mafic-ultramafic terrain*

The ratio image BR6/5 is useful for the delineation of forest zone underlined by felspathic gneiss (Qfg)/charnockite (Ch), and mafic-ultramafic rocks. The Qfg/Ch shows a light grey tonal contrast with a smooth texture. The mafic-ultramafic rocks show a moderate grey with relief features. The Hbg and Gr combinedly show similar spectral signatures with high reflectance. The presence of quartz and feldspar as common minerals in gneiss and granite may reflect the same spectral output in the image. The ratio image BR4/3 shows moderate grey, dark relief feature and bright signature, respectively for feldspathic gneiss/charnockite, mafic-ultramafic complex and combination gneiss and granites. The OLI ratioed outputs were used for the generation of colour composite images. Out of various composite images, the colour combination of BR6/4, 6/2 and 7/6; BR5/4, 6/3 and 4/2; BR5/3, 6/4 and 5/4, BR6/5, 4/3 and 2/1; and BR5/2, 3/2 and 7/2 were identified as suitable composite images for the interpretation of rock types in the study area (Fig. 9).

The composite image BR6/4, 6/2 and 7/6 show contrast spectral signature for mafic-ultramafic rocks along with prominent relief features (Fig. 9A).

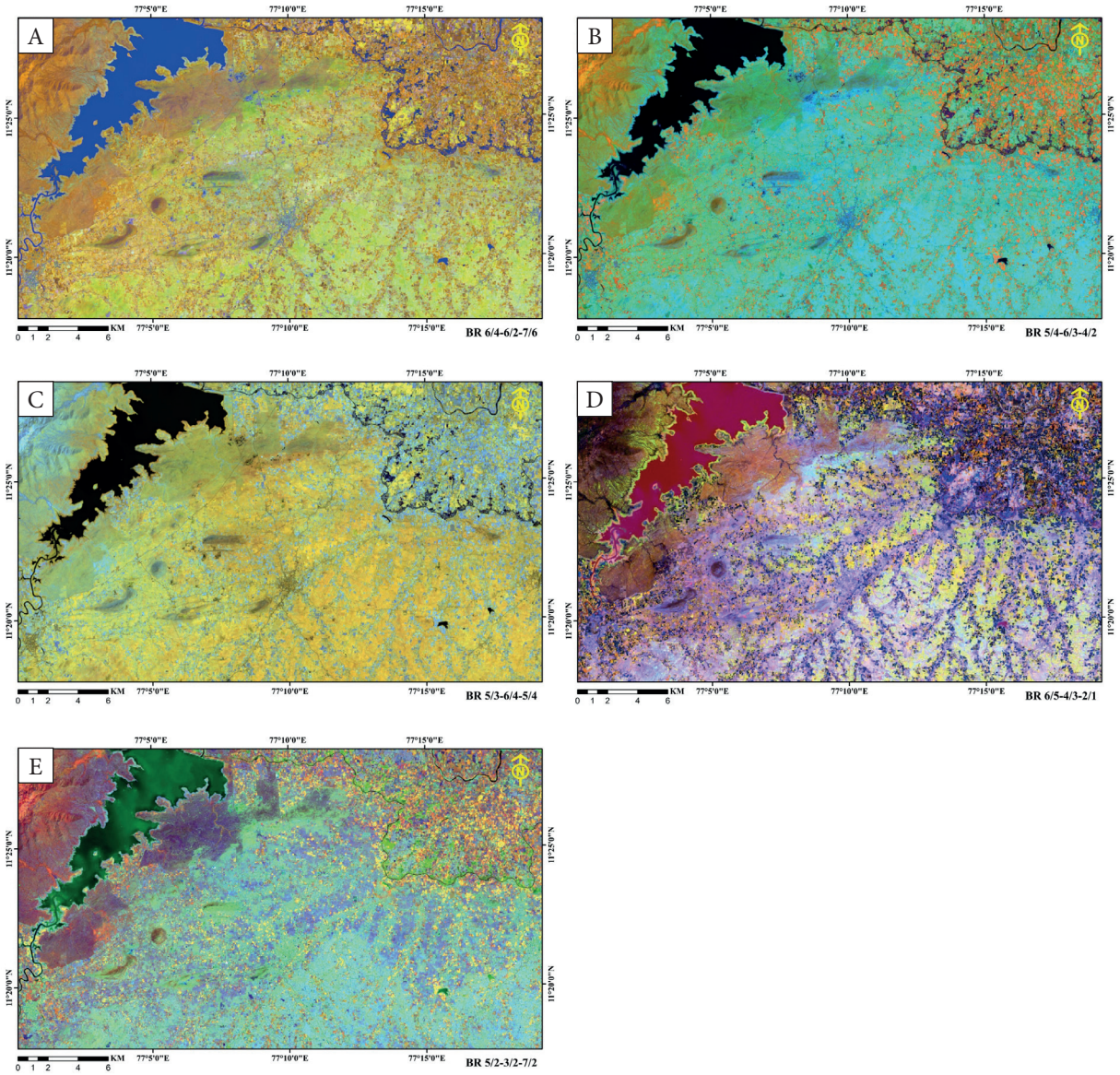

Fig. 9. *Colour composite images of band ratios derived from Landsat-8 OLI bands: A) BR 6/4, 6/2 and 7/6; B) BR 5/4, 6/3 and 4/2; C) BR 5/3, 6/4 and 5/4; D) BR 6/5, 4/3 and 2/1; E) BR 5/2, 3/2 and 7/2*

This composite image also exposes the surface-level outcropping of mafic-ultramafic rocks to some extent. The boundary condition of felspathic gneiss/charnockite is enhanced in an olive green colour. Though hornblende biotite gneiss and granite show similar spectral signatures, high reflectance with a lemon green contrast colour was noticed with granite formation. In the BR5/4, 6/3 and 4/2 ratio combination, once again the mafic-ultramafic complex is highlighted prominently (Fig. 9B). The BR5/3, 6/4 and 5/4 show contrast spectral signatures for mafic-ultramafic rocks charnockites and gneiss/granites (Fig. 9C). The BR5/2, 3/2 and 7/2 colour composite image support discrimination of mafic-ultramafic, intermediate (quartzo feldspathic gneiss)/charnockite and felsic (hornblende biotite gneiss and granite) formation (Fig. 9E). The BR6/5, 4/3 and 2/1 provide contrast spectral signatures for all rock types in the study area (Fig. 9D).

SVM classified output

In recent years, SVM classification of remotely sensed data has been utilized for improved lithological classification (Yu et al. 2012, Othman & Gloaguen 2014, Shebl et al. 2021). Similarly, in the present study, the SVM classified output provides a contrast spectral signature for various rock types compared to other processed outputs. The SVM is the only processed output in this study that provides enhanced output for both the surface-level and elevated outcrop of mafic-ultramafic rock types. This processed output is important in terms of PGE exploration since it helps to map mafic-ultramafic rocks in particular. The mafic-ultramafic rocks in this complex region are already identified as host rocks for PGE mineralization. In the SVM classified output, the mafic-ultramafic rocks, granites, hornblende biotite gneiss, quartzo feldspathic gneiss and charnockite were shown in a dark green, coral, blue, rome and light green colours, respectively (Fig. 10). The charnockite formation in the eastern part is concealed by thick cultivation practices and not highlighted in the SVM output. The water body in the reservoir and vegetation/forest cover, respectively, are shown in the sky blue and red colours.

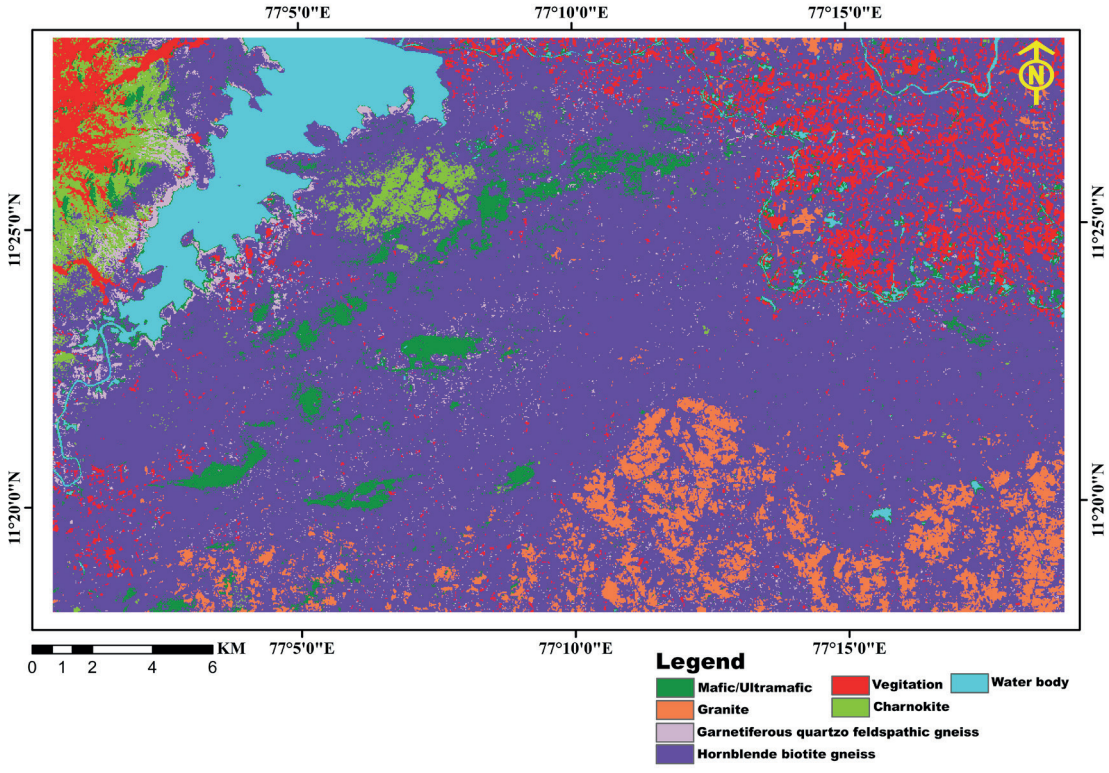

Fig. 10. *Support vector machine (SVM) classified Landsat-8 OLI satellite data output*

Characterizing reflectance spectra

The XRF analysis revealed that the percentage of silica content in the rock samples varies from 46.30% to 70.50%, representing mafic to felsic compensation. The major oxides in the rocks are useful in comparison with spectral features. The continuum spectra were plotted for all rock types using Origin Pro 8.5 software (Fig. 11).

The continuum spectra for different rock types show a minor variation in the percentage of the reflectance spectra; otherwise, these plots do not help extract absorption bands. The spectra of hornblende biotite gneiss show the albedo (reflectance) ranging from 24% in UV to 54% in the SWIR region. In the visible spectrum, the albedo increased slightly (35%) at 600 nm and then decreased (30%) at 700 nm. The spectra of meta-gabbro fall in the range of 14% to 41%, which show low albedo than the granitic gneiss. The meta-pyroxenite shows absorption features in the IR region. The albedo ranges from 21% in UV to 43% in the SWIR region. The gabbroic anorthosite shows higher albedo (33% to 67%) than any other rock types in the study area. The chromitite and meta-gabbro show similar spectral behaviour. The continuum removed spectra were plotted for extraction of absorption bands and characterization of the spectral behaviour of different rock types in the study area. The continuum-removed spectra of hornblende biotite gneiss show eight absorption features in a different part of the spectrum (Fig. 12A). The weak asymmetrical absorption at 750 nm is due to the electronic transition of ferrous to ferrous iron. The strong symmetrical absorption noticed at 1185 nm may be due to the presence of a minor amount of Fe^{2+} in plagioclase feldspar.

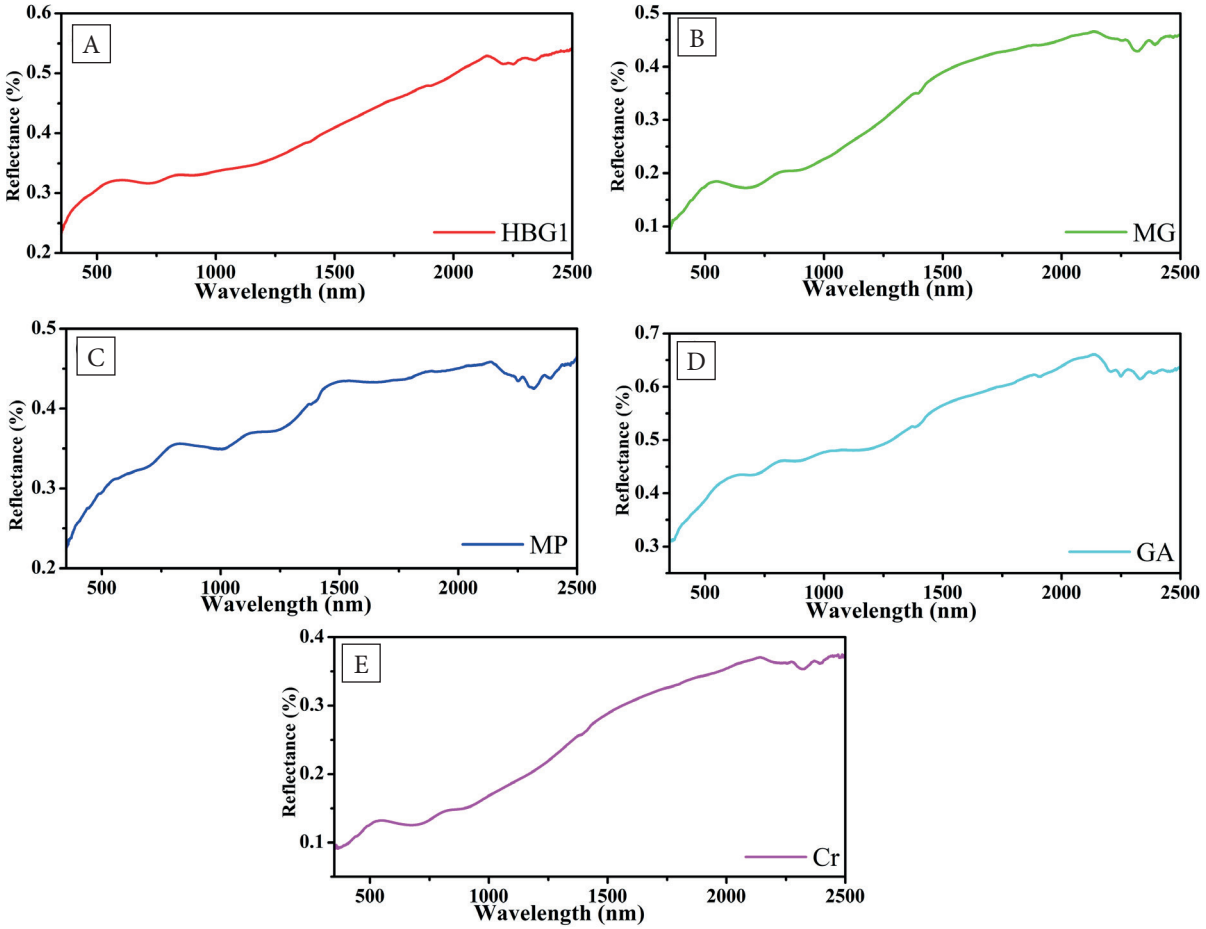

Fig. 11. *Reflectance spectra of hornblende biotite gneiss (A), meta-gabbro (B), meta-pyroxenite (C), gabbroic anorthosite (D) and chromitite (E). The spectra are plotted in continuum mode*

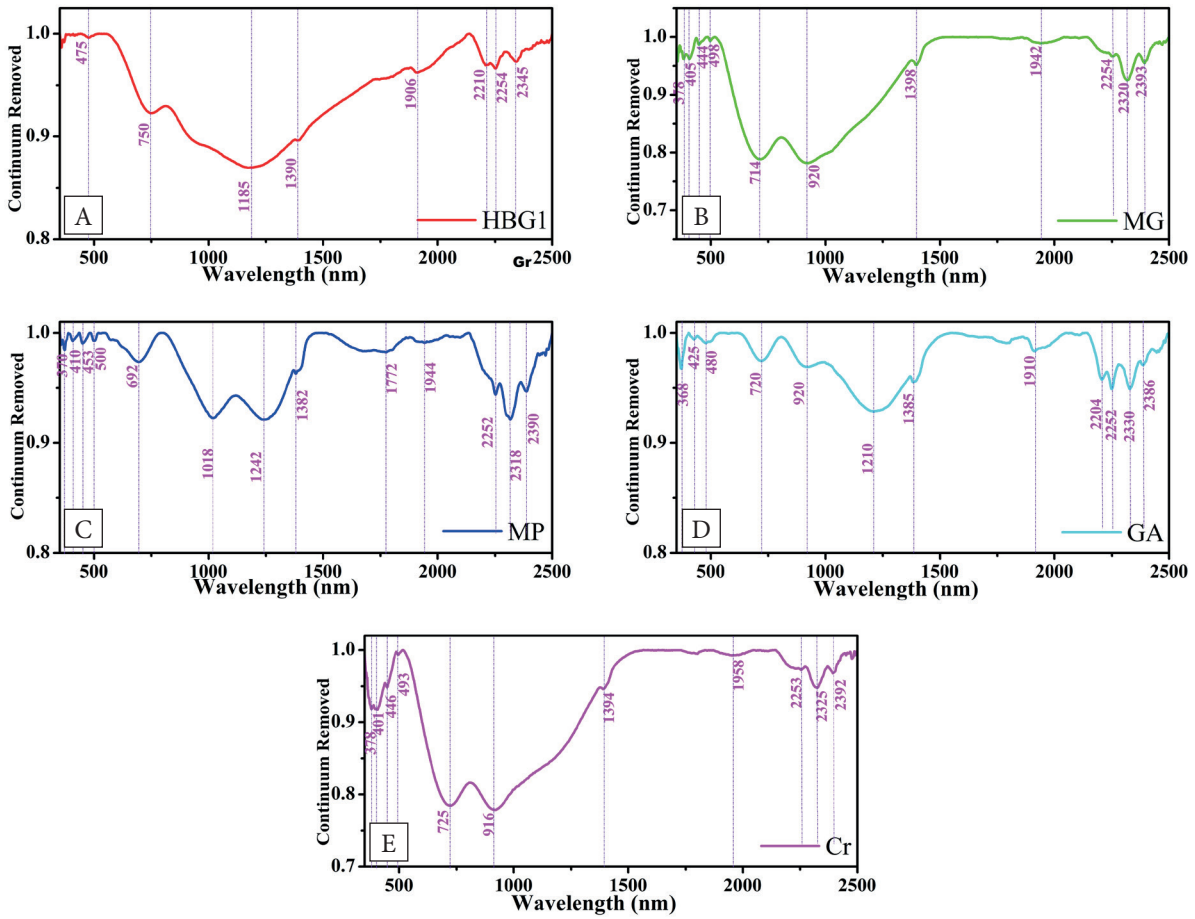

Fig. 12. *Continuum removed reflectance spectra of hornblende biotite gneiss (A), meta-gabbro (B), meta-pyroxenite (C), gabbroic anorthosite (D) and chromitite (E)*

The very weak absorptions noticed at 1390 nm and 1906 nm are due to the presence of a minor amount of hydroxyl and ferrous ions in the rock sample. The very weak to weak absorptions in the SWIR at 2210 nm, 2254 nm, and 2345 nm is due to the presence of Al-OH, Fe-OH and Mg-OH vibration spectra. The chemistry of hornblende biotite gneiss represent intermediate felsic composition with SiO_2 70.50%. The composition of other major oxides includes Al_2O_3 14.60%, CaO 3.08%, MgO 0.70% and Fe_2O_3 3.27% (Table 3).

A strong asymmetric absorption was observed at 920 nm in meta-gabbro due to the presence of iron-rich pyroxene minerals (Fig. 12B). The XRF result reveals that the chemistry of meta-gabbro is dominated by mafic composition such as SiO_2 46.30%, CaO 13.30% (Table 3). The ferromagnesian component (MgO 6.59%, and Fe_2O_3 15.50%) is significantly represented in the meta-gabbro. The Fe^{2+} – Fe^{3+} intervalence charge transfer leads to strong absorption at 714 nm in meta-gabbro. The absorptions due to the electronic processes in the UV-visible region (350–500 nm) are insignificant. In the SWIR spectrum, the absorption features at 2254 nm, 2320 nm, and 2393 nm in the meta-gabbro show the vibration spectra of Al-OH, Fe-OH and Mg-OH and the presence of alteration minerals like clinochlore, actinolite, and amphibolite.

In meta-pyroxenite, very weak absorptions are noticed in the UV-blue band spectrum, which is mostly insignificant (Fig. 12C). The meta-pyroxenite sample shows strong absorption at 1018 nm and 1242 nm, respectively, due to the presence of calcic pyroxene and FeO content in plagioclase minerals. Once again, the strong absorption at 2318 nm shows the presence of the

alteration mineral antigorite in the sample. The moderate absorption bands at 2252 nm and 2390 nm are due to Mg-OH vibration spectra of alteration minerals like clinochlore and amphibole. Meta-pyroxenite is one of the important rocks in the study area and is considered a host rock for PGE mineralization. The chemical analysis shows its mafic composition as SiO_2 47.30%, MgO 8.12%, CaO 10.90%, and Fe_2O_3 13.70% (Table 3).

The spectra obtained from the powder samples of gabbroic anorthosite show contrast absorption features in the UV, visible, IR and SWIR regions (Fig. 12D). The weak to moderate absorption at 425 nm, 480 nm, and 720 nm in the visible region indicate an electronic process in the metal ions. The moderate absorption at 920 nm is due to the low calcic pyroxene in the sample. The strong absorption at 1210 nm in the gabbroic anorthosite shows the presence of plagioclase feldspar with a minor amount of FeO content. The weak to moderate absorption features noticed at 2204 nm, 2252 nm, 2330 nm, and 2386 nm are due to the presence of alteration minerals with Al-OH, Fe-OH and Mg-OH vibration spectra. Since these absorption features are closely associated, providing a broad and overlapping absorption in the spectral range. The chemistry of the gabbroic anorthosite represents the felsic composition with a SiO_2 content of 60.10%. The ferromagnesium compositions are (MgO 3.14% and Fe_2O_3 5.12%) comparatively lower than the other mafic rocks. The chromitite rock sample shows prominent absorption bands at 401 nm, and 725 nm, respectively, due to the presence of Cr/Mn and Fe^{2+} – Fe^{3+} iron charge transfer absorptions (Fig. 12E). The strong symmetrical absorption at 916 nm reveals that the presence of low calcic pyroxenes in the sample. The weak absorptions in the SWIR spectral range (2253 nm, 2325 nm, and 2392 nm) are due to the vibration spectra and indicate a minor amount of alteration minerals in the rock.

CONCLUSION

Landsat-8 OLI satellite data was used for the interpretation of different rock types in the mafic-ultramafic terrain of the Bhavani complex in southern India. The identification of certain rock types like meta-gabbro, meta-pyroxenite, and chromitite is economically important since these rocks are considered host rocks for the platinum group of minerals. In this context, the present remote sensing-based study plays a vital role in mapping such rock types. The FCC of OLI data provides contrast spectral signatures for different rock types. Of the various colour composite images, composite images like B567, B456, and B457 are suitable for mapping both felsic and mafic composition in the study area. Of these three outputs, the composite image B457 is useful in mapping the surface level outcropping of the mafic-ultramafic (M/Um) formation. The colour composite images derived from the principal component analysis gave enhanced spectral variation between different rock types, particularly in PC312 and PC456. The PC456 support for interpretation of the mafic-ultramafic suite exposed at surface-level condition. The grey scales band ratios images like BR6/5 and BR4/3 provide quality support for mapping different rock types. The colour composite images like BR6/4-6/2-7/6, BR5/4-6/3-4/2, BR5/3-6/4-5/4, BR6/5-4/3-2/1, and BR5/2-3/2-7/2 derived from the ratioed output were useful in the delineation of various rock types. The SVM classified output supports the identification of different rock types, water bodies, and vegetation. SVM classified output of various processed data provides an enhanced spectral signature for the surface-level outcrop of mafic-ultramafic rocks and is thus considered one of the best tools for rock-type classification. The reflectance spectra of various rock types provide diagnostic absorption features, useful for differentiating the elemental composition and minerals. The presence of iron-rich and low calcic pyroxene, plagioclase feldspar and alteration minerals such as clinochlore, actinolite, antigorite, and amphiboles influence absorption in the rocks.

The authors would like to thank the Department of Science & Technology, Government of India, for sanctioning the research project (Sanction No. BDID/01/23/2014-HSRS) under the network project on Big Data Analytics-Hyperspectral Data. XRF analysis and Lab Spectral measurements were conducted at IIT Bombay, Department of Earth Science.

REFERENCES

Abdeen M.M., Allison T., Abdelsalam M.G. & Stern R.J., 2001. Application of ASTER band-ratio images for geological mapping in arid regions; the Neoproterozoic Allaqi Suture, Egypt. *Abstract with Program Geological Society of America*, 3(3), 289.

Abdelsalam M.G., Stern R.J. & Berhane W.G., 2000. Mapping gossans in arid regions with Landsat TM and SIR-C images: the Beddaho Alteration Zone in northern Eritrea. *Journal of African Earth Sciences*, 30(4), 903–916. https://doi.org/10.1016/S0899-5362(00)00059-2.

Abrams M.J., 1984. Landsat-4 thematic mapper and thematic mapper simulator data for 1 a porphyry copper deposit. *Photogrammetric Engineering and Remote Sensing*, 50(8), 1171–1173.

Abrams M.J., Brown D., Lepley L. & Sadowski R., 1983. Remote sensing for porphyry copper deposits in southern Arizona. *Economic Geology*, 78(4), 591–604. https://doi.org/10.2113/gsecongeo.78.4.591.

Amer R., Kusky T. & Ghulam A., 2010. Lithological mapping in the Central Eastern Desert of Egypt using ASTER data. *Journal of African Earth Sciences*, 56(2–3), 75–82. https://doi.org/10.1016/j.jafrearsci.2009.06.004.

Anbazhagan S., Biswal T.K., Roy T. & Kusuma K.N., 2006. Remote sensing study of granulitic terrain in parts of Gujarat and Rajasthan. *Journal of the Indian Society of Remote Sensing*, 34(4), 331–341. https://doi.org/10.1007/BF02990918.

Anbazhagan S., Sainaba N.K. & Arivazhagan S., 2012. Remote sensing study of Sittampundi anorthosite complex, India. *Journal of the Indian Society of Remote Sensing*, 40(1), 145–153. https://doi.org/10.1007/s12524-011-0126-y.

Beauchemin M. & Fung K.B., 2001. On statistical band selection for image visualization. *Photogrammetric Engineering and Remote Sensing*, 67(5), 571–574.

Bernstein L.S., Jin X., Gregor B. & Adler-Golden S.M., 2012. Quick atmospheric correction code: algorithm description and recent upgrades. *Optical Engineering*, 51(11), 111719. https://doi.org/10.1117/1.OE.51.11.111719.

Bhan S., Bhattacharya A., Guha P. & Ravindran K., 1991. IRS-1A applications in geology and mineral resources. *Current Science*, 61(3–4), 247–251.

Bhattacharya S., 2010. Review: the charnockite problem, a twenty-first century perspective. *Natural Science*, 2(1), 402–408. https://doi.org/10.4236/ns.2010.24049.

Bhattacharya S., Majumdar T.J., Rajawat A.S., Panigrahy M.K. & Das P.R., 2012. Utilization of Hyperion data over Dongargarh, India, for mapping altered/weathered and clay minerals along with field spectral measurements. *International Journal of Remote Sensing*, 33(17), 5438–5450. https://doi.org/10.1080/01431161.2012.661094.

Buchanan M.D., 1979. Effective utilization of colour in multidimensional data presentations. [in:] Parsons J.R. (ed.), *Advances in Display Technology*, Proceedings of SPIE, 0199, Society of Photo-Optical Instrumentation Engineers, 9–18. https://doi.org/10.1117/12.958037.

Chavez P.S. Jr., Berlin G.L. & Sowers L.B., 1982. Statistical method for selecting Landsat MSS ratios. *Journal of Applied Photographic Engineering*, 8(1), 23–30.

Chavez P.S., Guptill S.C. & Bowell J.A., 1984. Image processing techniques for thematic mapper data. [in] *Technical Paper of the Annual Meeting ASP ACSM Convention. Volume 2*, ACSM-ASPRS Technical Papers, American Society of Photogrammetry, Washington, 728–742.

Chavez P., Sides S.C. & Anderson J.A., 1991. Comparison of three different methods to merge multiresolution and multispectral data: Landsat TM and SPOT panchromatic. *Photogrammetric Engineering and Remote Sensing*, 57(3), 295–303.

Chellamuthu Ranganathan P. & Siddan A., 2021. Application of spectral signature to analyze quality of magnesite ore mineral deposits and altered rocks of Salem, India. *Arabian Journal of Geosciences*, 14(7), 651. https://doi.org/10.1007/s12517-021-06963-1.

Ciampalini A., Garfagnoli F., Antonielli B., Moretti S. & Righini G., 2013. Remote sensing techniques using Landsat ETM+ applied to the detection of iron ore deposits in Western Africa. *Arabian Journal of Geosciences*, 6(11), 4529–4546. https://doi.org/10.1007/s12517-012-0725-0.

Clark R.N., 1999. Spectroscopy of rocks and minerals, and principles of spectroscopy. [in:] Rencz A.N. (ed.), *Remote Sensing for the Earth Sciences: Manual of Remote Sensing, Volume 3*, 3rd ed., John Wiley and Sons, New York, 3–58.

Crane R., 1971. Propagation phenomena affecting satellite communication systems operating in the centimeter and millimeter wavelength bands. *Proceedings of the IEEE*, 59(2), 173–188. https://doi.org/10.1109/PROC.1971.8123.

Crósta A.P. & Moore J., 1990. Ehancement of LANDSAT Thematic Mapper imagery for residual soil mapping in SW Minas Gerais State, Brazil: A prospecting case history in Greenstone belt terrain. [in:] *Proceedings of the Seventh Thematic Conference on Remote Sensing for Exploration Geology: Methods,Integration, Solutions: October 2–6, 1989, Calgary, Alberta, Canada. Volume II*, Environmental Research Institute of Michigan, 1173–1187.

Drury S., 1990. SPOT image data as an aid to structural mapping in the southern Aravalli Hills of Rajasthan, India. *Geological Magazine*, 127(3), 195–207. https://doi.org/10.1017/S0016756800014485.

Evans D., 1988. Multisensor classification of sedimentary rocks. *Remote Sensing of Environment*, 25(2), 129–144. https://doi.org/10.1016/0034-4257(88)90097-1.

Gad S. & Kusky T., 2007. ASTER spectral ratioing for lithological mapping in the Arabian–Nubian shield, the Neoproterozoic Wadi Kid area, Sinai, Egypt. *Gondwana Research*, 11(3), 326–335. https://doi.org/10.1016/j.gr.2006.02.010.

Gahlan H. & Ghrefat H., 2018. Detection of Gossan Zones in Arid Regions using Landsat 8 OLI data: Implication for mineral exploration in the Eastern Arabian Shield, Saudi Arabia. *Natural Resources Research*, 27(1), 109–124. https://doi.org/10.1007/s11053-017-9341-8.

Glikson A. & Creasey J., 1995. Application of Landsat-5 TM imagery to mapping of the Giles Complex and associated granulites, Tomkinson Ranges, western Musgrave Block, central Australia. *AGSO Journal of Australian Geology and Geophysics*, 16(1), 173.

Goetz A.F. & Rowan L.C., 1981. Geologic remote sensing. *Science*, 211(4484), 781–791. https://doi.org/10.1126/science.211.4484.781.

Gopalakrishnan R. & Shanmugam P., 1995. *Reconnaissance Survey for Platinum Group of Elements in Ultrabasic-Ultramafic rocks of Solavanur-Mallanayakkanpalaiyam-Karappadi areas, Periyar District*. GSI Progress Report for the FS 1993-94.

Gupta R.P., 2017. *Remote Sensing Geology*. Springer, Berlin, Heidelberg.

Holben B. & Justice C., 1981. An examination of spectral band ratioing to reduce the topographic effect on remotely sensed data. *International Journal of Remote Sensing*, 2(2), 115–133. https://doi.org/10.1080/01431168108948349.

Huang C., Song K., Kim S., Townshend J.R., Davis P., Masek J.G. & Goward S.N., 2008. Use of a dark object concept and support vector machines to automate forest cover change analysis. *Remote Sensing of Environment*, 112(3), 970–985. https://doi.org/10.1016/j.rse.2007.07.023.

Jensen J.R., 1996. *Introductory Digital Image Processing: A Remote Sensing Perspective*. Prentice Hall, Hoboken.

Kamel M., Abdeen M.M., Youssef M.M., Orabi A.M. & Abdelbaky E., 2022. Utilization of Landsat-8 (OLI) image data for geological mapping of the neo-Proterozoic basement rocks in the Central Eastern Desert of Egypt. *Journal of the Indian Society of Remote Sensing*, 50(3), 469–492. https://doi.org/10.1007/s12524-021-01465-9.

Kaufmann H., 1988. Mineral exploration along the Aqaba-Levant Structure by use of TM-data: Concepts, processing and results. *International Journal of Remote Sensing*, 9(10–11), 1639–1658. https://doi.org/10.1080/01431168808954966.

Krishnamurthy J., 1997. The evaluation of digitally enhanced Indian Remote Sensing Satellite (IRS) data for lithological and structural mapping. *International Journal of Remote Sensing*, 18(16), 3409–3437. https://doi.org/10.1080/014311697216955.

Kumar C., Shetty A., Raval S., Sharma R. & Ray P.C., 2015. Lithological discrimination and mapping using ASTER SWIR Data in the Udaipur area of Rajasthan, India. *Procedia Earth and Planetary Science*, 11, 180–188. https://doi.org/10.1016/j.proeps.2015.06.022.

Kusuma K.N., Ramakrishnan D. & Pandalai H.S., 2012. Spectral pathways for effective delineation of high-grade bauxites: A case study from the Savitri River Basin, Maharashtra, India, using EO-1 Hyperion data. *International Journal of Remote Sensing*, 33(22), 7273–7290. https://doi.org/10.1080/01431161.2012.700131.

Loughlin W., 1991. Principal component analysis for alteration mapping. *Photogrammetric Engineering and Remote Sensing*, 57(9), 1163–1169.

Maheswaran S.U., Anbazhagan S., Tamilarasan K., Kasilingam C. & Chinnamuthu M., 2019. Lithology and structural mapping of Kadavur Basin, Tamil Nadu, India, using IRS P6 LISS III satellite data. *Journal of the Indian Society of Remote Sensing*, 47(8), 1275–1286. https://doi.org/10.1007/s12524-019-00989-5.

Mwaniki M.W., Moeller M.S. & Schellmann G., 2015. A comparison of Landsat 8 (OLI) and Landsat 7 (ETM+) in mapping geology and visualizing lineaments: A case study of central region Kenya. *International Archives of the Photogrammetry, Remote Sensing & Spatial Information Sciences*, XL-7/W3(7), 897–903. https://doi.org/10.5194/isprsarchives-XL-7-W3-897-2015.

Othman A.A. & Gloaguen R., 2014. Improving lithological mapping by SVM classification of spectral and morphological features: The discovery of a new chromite body in the Mawat ophiolite complex (Kurdistan, NE Iraq). *Remote Sensing*, 6(8), 6867–6896. https://doi.org/10.3390/rs6086867.

Pal M. & Mather P.M., 2005. Support vector machines for classification in remote sensing. *International Journal of Remote Sensing*, 26(5), 1007–1011. https://doi.org/10.1080/01431160512331314083.

Pour A.B., Park Y., Park T.-Y.S., Hong J.K., Hashim M., Woo J. & Ayoobi I., 2018. Regional geology mapping using satellite-based remote sensing approach in Northern Victoria Land, Antarctica. *Polar Science*, 16, 23–46. https://doi.org/10.1016/j.polar.2018.02.004.

Prabhakar J., Boopathi D. & Kumar S.B.V., 2012. *Investigation for Platinum Group of elements by scout drilling in Solavanur and Karappadi blocks and detailed mapping in Mallanayakkanpalaiyam block, Mettuppalaiyam mafic-ultramafic complex, Tamil Nadu*. Geological Survey of India Report.

Prinz T., 1996. Multispectral remote sensing of the Gosses Bluff impact crater, central Australia (NT) by using Landsat-TM and ERS-1 data. *ISPRS Journal of Photogrammetry and Remote Sensing*, 51(3), 137–149. https://doi.org/10.1016/0924-2716(95)00007-0.

Rao Y.J.B., Chetty T.R.K., Janardhan A.S. & Gopalan K., 1996. Sm-Nd and Rb-Sr ages and P-T history of the Archean Sittampundi and Bhavani layered meta-anorthosite complexes in Cauvery shear zone, South India: Evidence for Neoproterozoic reworking of archean crust. *Contributions to Mineralogy and Petrology*, 125(2–3), 237–250. https://doi.org/10.1007/s004100050219.

Roy D.P., Wulder M.A., Loveland T.R., Woodcock C.E., Allen R.G., Anderson M.C., Helder D. et al., 2014. Landsat-8: Science and product vision for terrestrial global change research. *Remote Sensing of Environment*, 145, 154–172. https://doi.org/10.1016/j.rse.2014.02.001.

Ruiliang P., 2017. *Hyperspectral Remote Sensing: Fundamentals and Practices*. CRC Press, Boca Raton.

Ruiz-Armenta J. & Prol-Ledesma R., 1998. Techniques for enhancing the spectral response of hydrothermal alteration minerals in Thematic Mapper images of Central Mexico. *International Journal of Remote Sensing*, 19(10), 1981–2000. https://doi.org/10.1080/014311698215108.

Sabins F.F., 1999. Remote sensing for mineral exploration. *Ore Geology Reviews*, 14(3–4), 157–183. https://doi.org/10.1016/S0169-1368(99)00007-4.

Satterwhite M., 1984. *Discriminating vegetation and soils using Landsat MSS and Thematic Mapper bands and band ratios*. Army Engineer Topographic Labs Fort, Belvoir.

Satyanarayanan M., Balaram V., Sylvester P., Rao D.S., Charan S., Shaffer M., Dar A.M. & Anbarasu K., 2011. Geochemistry of late-archean Bhavani (Mettupalayam) mafic/ultramafic complex, Southern India: Implications for platinum group element mineralization. *Journal of Applied Geochemistry*, 13(1), 1–14.

Scheunders P., Tuia, D. & Moser G., 2018. Contributions of machine learning to remote sensing data analysis. [in:] Shunlin L. (ed.), *Comprehensive Remote Sensing. Volume 2: Data Processing and Analysis Methodology*, Elsevier, 199–243, https://doi.org/10.1016/B978-0-12-409548-9.10343-4.

Shebl A., Abdellatif M., Hissen M., Abdelaziz M.I. & Csámer Á., 2021. Lithological mapping enhancement by integrating Sentinel 2 and gamma-ray data utilizing support vector machine: A case study from Egypt. *International Journal of Applied Earth Observation and Geoinformation*, 105, 102619. https://doi.org/10.1016/j.jag.2021.102619.

Su L. & Huang Y., 2009. Support Vector Machine (SVM) classification: Comparison of linkage techniques using a clustering-based method for training data selection. *GIScience & Remote Sensing*, 46(4), 411–423. https://doi.org/10.2747/1548-1603.46.4.411.

Sultan M., Arvidson R.E., Sturchio N.C. & Guinness E.A., 1987. Lithologic mapping in arid regions with Landsat thematic mapper data: Meatiq dome, Egypt. *Geological Society of America Bulletin*, 99(6), 748–762. https://doi.org/10.1130/0016-7606(1987)99<748:LMIARW>2.0.CO;2.

Tamilarasan K., Anbazhagan S., Maheswaran S., Ranjithkumar S., Kusuma K. & Rajesh V., 2022. Reflectance spectra and AVIRIS-NG airborne hyperspectral data analysis for mapping ultramafic rocks in igneous terrain. *Journal of Spectral Imaging*, 11(1), a9. https://doi.org/10.1255/jsi.2022.a9.

Vapnik V., 1995. *The Nature of Statistical Learning Theory*. Springer Science & Business Media.

Yesou H., Besnus Y. & Rolet J., 1993. Extraction of spectral information from Landsat TM data and merger with SPOT panchromatic imagery – a contribution to the study of geological structures. *ISPRS Journal of Photogrammetry and Remote Sensing*, 48(5), 23–36. https://doi.org/10.1016/0924-2716(93)90069-Y.

Yu L., Porwal A., Holden E.-J. & Dentith M.C., 2012. Towards automatic lithological classification from remote sensing data using support vector machines. *Computers & Geosciences*, 45, 229–239. https://doi.org/10.1016/j.cageo.2011.11.019.

Zhang X., Pamer M. & Duke N., 2007. Lithologic and mineral information extraction for gold exploration using ASTER data in the south Chocolate Mountains (California). *ISPRS Journal of Photogrammetry and Remote Sensing*, 62(4), 271–282. https://doi.org/10.1016/j.isprsjprs.2007.04.004.